Shape-Controlled Synthesis of Isotopic Yttrium-90-Labeled Rare Earth Fluoride Nanocrystals for Multimodal Imaging

Taejong Paik,[†] Ann-Marie Chacko,[‡,§,#] John L. Mikitsh,[‡] Joseph S. Friedberg,[∥] Daniel A. Pryma,[‡] and Christopher B. Murray*[,†,⊥]

[†]Department of Chemistry, [‡]Division of Nuclear Medicine and Clinical Molecular Imaging, Department of Radiology, [§]Institute for Translational Medicine and Therapeutics, Perelman School of Medicine, [∥]Division of Thoracic Surgery, and [⊥]Department of Materials Science and Engineering, University of Pennsylvania, Philadelphia, Pennsylvania 19104, United States. [#]Present address: Laboratory for Translational and Molecular Imaging, Cancer & Stem Cell Biology Program, Duke-NUS Graduate Medical School, Singapore, 169857.

ABSTRACT Isotopically labeled nanomaterials have recently attracted much attention in biomedical research, environmental health studies, and clinical medicine because radioactive probes allow the elucidation of *in vitro* and *in vivo* cellular transport mechanisms, as well as the unambiguous distribution and localization of nanomaterials *in vivo*. In addition, nanocrystal-based inorganic materials have a unique capability of customizing size, shape, and composition; with the potential to be designed as multimodal imaging probes. Size and shape of nanocrystals can directly influence interactions with biological systems, hence it is important to develop synthetic methods to design radiolabeled nanocrystals with precise control of size and shape. Here, we report size- and shape-controlled synthesis of rare earth fluoride nanocrystals doped with the β-emitting radioisotope yttrium-90 (^{90}Y). Size and shape of nanocrystals are tailored *via* tight control of reaction parameters and the type of rare earth hosts (*e.g.*, Gd or Y) employed. Radiolabeled nanocrystals are synthesized in high radiochemical yield and purity as well as excellent radiolabel stability in the face of surface modification with different polymeric ligands. We demonstrate the Cerenkov radioluminescence imaging and magnetic resonance imaging capabilities of ^{90}Y-doped GdF_3 nanoplates, which offer unique opportunities as a promising platform for multimodal imaging and targeted therapy.

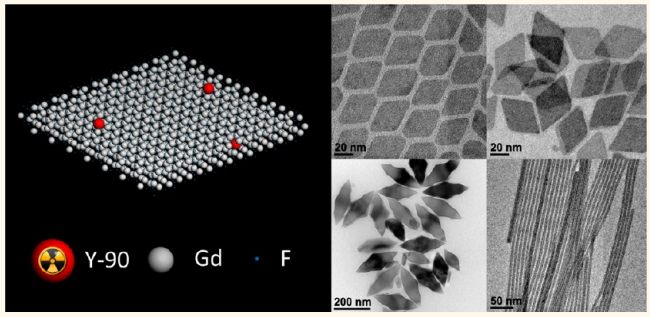

KEYWORDS: yttrium-90 · radioluminescence · Cerenkov luminescence · MRI · GdF_3 · nanoplate

Nanocarrier platforms, designed as imaging agents, serve an important role in biomedical research for the study of biological processes and transport mechanisms[1−3] as well as in clinical medicine for early and accurate disease detection.[4−6] A variety of imaging modalities such as optical, magnetic, and nuclear have been utilized in different applications according to sensitivity and contrast, depth of signal penetration, and spatial and temporal resolution.[7] Among them, imaging with radiolabeled probes has attracted much attention due to high sensitivity and noninvasive detection of subpicomolar concentrations of radionuclides.[8] Radiolabeled probes offer information on pharmacokinetics, probe distribution and localization, *in vitro* and *in vivo* transport mechanisms, and medical diagnosis with support by quantitative information calculated from radioactivity levels. Nanocrystal-based inorganic materials offer a great opportunity for designing multimodal imaging probes, implementing complementary detection capabilities into a single material.[9−11] Properties of highly uniform nanocrystals are easily tailored by customizing elemental composition among noble metals,[12] magnetic materials,[13] semiconductors,[14] and phosphors,[15] with a choice of radioactive dopants, such as ^{64}Cu,[16,17] ^{59}Fe,[18] ^{56}Co,[19] ^{153}Sm,[20,21] ^{198}Au,[22] ^{125}I,[23] and ^{18}F.[24,25]

Among the different radioisotopes, ^{90}Y is particularly interesting as a nanocrystal dopant due to its unique properties. ^{90}Y is a pure β-emitter that yields one very high energy β-particle (E_{max} = 2.27 MeV, E_{mean} = 939 keV)

* Address correspondence to cbmurray@sas.upenn.edu.

Received for review November 13, 2014 and accepted August 8, 2015.

Published online August 08, 2015
10.1021/acsnano.5b03355

with each decay.[26] At high doses, ^{90}Y-labeled materials are most often utilized as therapeutic agents with high energy emissions that travel a limited distance *in vivo*, limiting off-target effects (maximum range in soft tissue is about 11 mm).[27] The half-life of ^{90}Y is 2.67 days and is sufficient for tracing biological processes over several days while still having sufficiently rapid decay to prevent protracted toxicity. Even as a pure β-emitter, the low yield Bremsstrahlung photons and annihilation photon pairs from ^{90}Y decay are detectable by nuclear imaging using SPECT and PET, respectively, albeit with low sensitivity.[28,29] However, another interesting property of ^{90}Y is its optical imaging capability; ^{90}Y is one of the most efficient radionuclides for stimulating Cerenkov luminescence.[30]

The lanthanide-based nanocrystals have tremendous potential for designing multimodal imaging probes.[31−34] Rare earth hosts are compatible with various radiolanthanides[20] and ^{18}F,[24,25] which enables incorporation of radioisotopes in the nanocrystal hosts. The f-block lanthanide elements exhibit unique optical and magnetic properties, including upconversion luminescence and paramagnetic behaviors, which can be further manipulated by control of size,[35,36] shape,[37] and compositions.[38,39] In addition, the size and shape of lanthanide-based nanocrystals can be precisely controllable.[40−44] Numerous reports indicate that the size and shape of nanocrystals also influence physiological interactions such as effects on cellular binding and internalization[45−49] and toxicity in biological systems.[50−53] Therefore, the development of synthetic methods to tailor the morphology of highly uniform radiolabeled nanocrystals will be important to aid the exploration of the transport and localization of shape-engineered nanomaterials and to evaluate their potential environmental and health benefits.

Here, we report size- and shape-controlled synthesis and characterization of radiolabeled rare earth fluoride nanocrystals. Fluoride-type materials are promising candidates due to their rich morphological diversity.[54−56] Anisotropic rare earth fluoride nanocrystals are synthesized *via* high-temperature thermal decomposition of rare earth precursors in the presence of yttrium-90 radiolanthanides. Higher temperature reaction conditions permit rapid nucleation and growth of uniform nanocrystals within an hour, thus minimizing the loss of radioactivity due to physical decay. By changing the reaction times, temperatures, and type of rare earth hosts (gadolinium or yttrium), highly uniform ^{90}Y-doped rare earth fluoride nanocrystals are synthesized with morphology tunable from nanoplates, nanowires, to bipyramids. Radiolabeled nanocrystals show excellent chemical stability of radioactivity toward surface chemical modifications. We investigated noninvasive nuclear and optical radioluminescence and MR relaxometry properties of these samples to support their potential as multimodal imaging applications.

RESULTS AND DISCUSSION

Shape-Controlled Synthesis of ^{90}Y-Labeled Rare Earth Fluoride Nanocrystals. Anisotropic rare earth fluoride nanocrystals are synthesized *via* high-temperature thermal decomposition of rare earth chloride precursors in the presence of lithium fluoride (LiF) and dopants depending on the intended application. $^{90}YCl_3$ is used as radiolanthanide precursors. In our studies, gadolinium chloride ($GdCl_3$) and yttrium chloride (YCl_3) are used as reaction precursors for host materials to maintain reactivity similar to that of $^{90}YCl_3$ radiodopants in the nucleation and growth process. ^{90}Y incorporates inside the host during the growth of nanocrystals, preventing radioisotope leakage from nanocrystals during *in vitro* and *in vivo* applications. These precursors are fluorinated using an excess of LiF, resulting in fluoride-based nanocrystals (GdF_3, YF_3, and $LiYF_4$). Under the reaction conditions employed, nanocrystals do not form without the addition of LiF, revealing that LiF participates not only in fluorinating the nanocrystals but also in facilitating the formation of nanocrystals.

Nanocrystal size and shape are readily controlled by modification of reaction time and temperature as well as the type of host materials. With $GdCl_3$ precursors, ellipsoidal GdF_3:^{90}Y/Y nanoplates are formed at 290 °C after a 20 min reaction (Figure 1a). Energy-dispersive X-ray spectroscopy (EDS) measurement reveals that nanocrystals are mainly composed of Gd and F elements (Figure 1d). At an increased reaction temperature (Figure 1b) or increased reaction time (Figure 1c), rhombic GdF_3:^{90}Y/Y nanoplates are obtained as final products with increasing the size of nanoplates. This trend is consistent with results previously reported without the addition of radioisotopes, even though $GdCl_3$ is used as a precursor in this study instead of standard gadolinium trifluoroacetate salts.[57] Using YCl_3 precursors instead of $GdCl_3$ and heating at 320 °C for 20 min results in a majority of YF_3 product having nanowire morphology with a small quantity of YF_3 rhombic nanoplates (Figure 1e,f), as confirmed by the single-crystalline pattern in fast Fourier transforms (FFT) of the high-resolution transmission electron microscopy (HRTEM) image and the wide-angle selected area electron diffraction (SAED) of nanowire bundles (Figure 2a,b). Nanowires reach several microns in length, but the width of an individual nanowire is approximately 4 nm on average. Increasing the reaction time to 40 min at the same temperature results in square bipyramidal-shaped $LiYF_4$:^{90}Y nanocrystals approximately 250 nm long and 90 nm wide on average, as displayed in transmission electron microscopy (TEM) and scanning electron microscopy (SEM) images (Figures 1g,h and 2c).

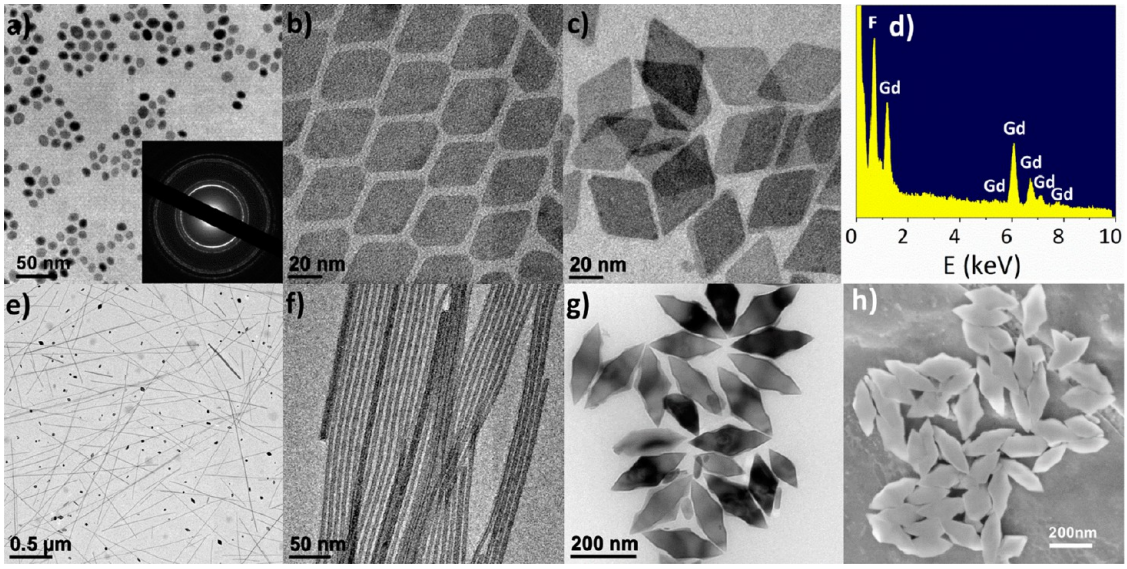

Figure 1. Characterization of Y-doped nanocrystals following full decay of ^{90}Y. TEM images of GdF_3:Y nanoplates formed under different reaction conditions: (a) ellipsoidal nanoplates (290 °C, 20 min) and rhombic nanoplates obtained at (b) 320 °C for 40 min or (c) 290 °C for 4 h. (d) EDS spectrum of GdF_3:Y nanoplates. (e−h) When YCl_3 is used as the precursor, YF_3 nanowires are obtained at 320 °C after 20 min (e,f), or bypiramidal $LiYF_4$ nanocrystals are synthesized at 320 °C for 40 min.

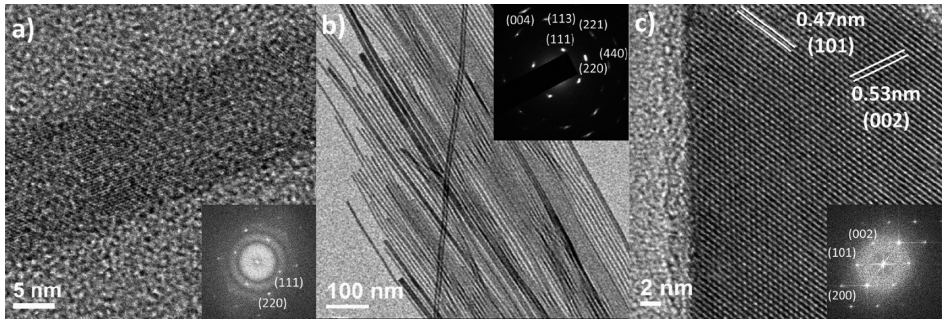

Figure 2. (a) HRTEM image and FFT pattern of a single YF_3 nanowire. (b) TEM image and wide-angle SAED pattern of nanowire bundles. Inset shows a single-crystalline electron diffraction pattern. (c) HRTEM image and FFT pattern of a $LiYF_4$ nanocrystal.

Radioactive thin layer chromatography (radioTLC) confirms that ^{90}Y is successfully incorporated into the nanocrystals in near quantitative yield, with no "free" or nonassociated ^{90}Y-labeled species identified in the crude reaction mixture (Figure 3 and Figure S1). To prepare water-dispersible nanocrystals, the surface of nanocrystals is modified with polyvinylpyrrolidone (PVP) polymeric ligands, and PVP-modified GdF_3:^{90}Y/Y nanoplates are analyzed by radioTLC to confirm the identity and purity of radioactive species after surface modification. As shown in Figure 3, intense radioactive signals are detected only at the TLC origin, whereas the presence of free ^{90}Y would have not been detected at the TLC solvent front, indicating chemical stability of the radioactivity toward surface chemical modifications. We can easily control the specific activity of the ^{90}Y-doped nanocrystals (*i.e.*, radioactivity (μCi)/nanocrystal mass (mg)) by varying the initial amount of $^{90}YCl_3$ added into the reaction system. Note that the amount of ^{90}Y added (1−4 mCi) translates to 0.003−0.01% of total host material added. Thus,

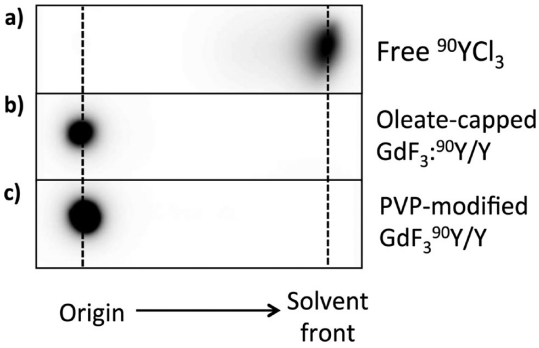

Figure 3. RadioTLC autoradiography images of (a) $^{90}YCl_3$ compared to (b) oleate-capped and (c) PVP-modified GdF_3:^{90}Y/Y, where free (*i.e.*, nonbound) ^{90}Y is detected at the solvent front and ^{90}Y bound to nanocrystal formulations remains at the TLC origin.

following full radioactive decay of ^{90}Y, the nanocrystal structure should remain intact because the majority Y dopant is not radioactive. This confirms that the ^{90}Y-doped GdF_3 nanoplates can be isolated in high radiochemical purity (>99%).

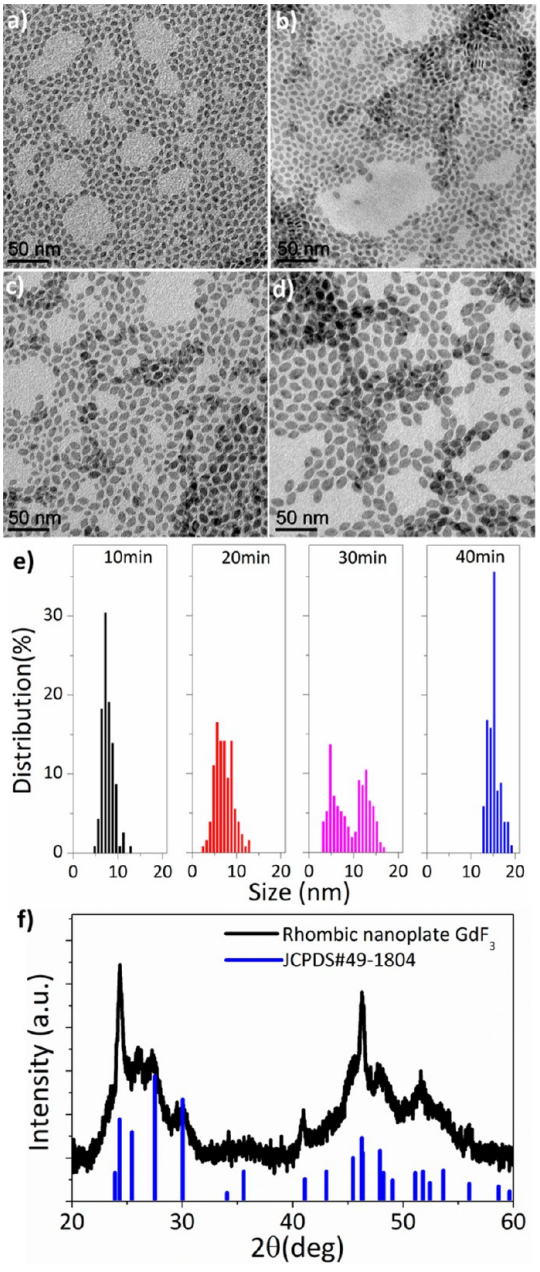

Figure 4. Size and morphology evolution of GdF_3 nanoplates during the reaction. TEM images at (a) 10 min, (b) 20 min, (c) 30 min, and (d) 40 min reaction times at 320 °C and (e) tip-to-tip size distribution histograms of GdF_3 nanoplates at 10, 20, 30, and 40 min reaction times. (f) PXRD pattern of GdF_3 nanoplates.

In order to understand the shape evolution of the nanocrystals, the identical reactions are conducted at a 320 °C reaction temperature without an addition of radioisotopes. Aliquots are taken during the reaction at 10 min intervals and analyzed by TEM and powder X-ray diffraction (PXRD). Figure 4 shows TEM images of GdF_3 nanoplates taken at 10, 20, 30, and 40 min reaction times (Figure 4a–d, respectively). TEM analysis reveals that ellipsoidal nanoplates are initially formed after 10 min with tip-to-tip distances of approximately 8.1 ± 1.2 nm (Figure 4a,e). After being aged at the same temperature (320 °C), Ostwald ripening is observed in which small nanoplates disappear and large plates continue to grow, yielding a bimodal size distribution of nanoplates (Figure 4b,c,e). With longer reaction times, the large nanoplates grow to form a rhombic morphology and the small nanoplates are consumed as reported in previous studies (Figure 4d,e).[58,59] After 40 min, small ellipsoidal nanoplates are completely replaced with nearly monodisperse rhombic nanoplates with tip-to-tip distances of 15.5 ± 1.3 nm (Figure 4d,e). To further understand the growth process, the small ellipsoidal nanoplates are first synthesized and purified to remove any unreacted monomers, and then the purified nanoplates are redispersed into the reaction mixtures containing oleic acid, octadecene, and lithium fluoride for further aging at 320 °C without Gd precursors.[60] Figure 5a shows the TEM image and the size histogram of ellipsoidal GdF_3 nanoplates added into the reaction mixtures. During the aging process, in the absence of Gd precursors, size defocusing is observed from uniform ellipsoidal nanoplates to smaller and larger nanoplates forming the bimodal size distribution, and finally, the nanoplates refocus into the unimodal large rhombic nanoplates, as displayed in Figure 5b–d. This trend reveals that the Ostwald ripening process indeed contributes to the growth from ellipsoidal nanoplates to rhombic nanoplates. Figure 4f displays a PXRD pattern of rhombic GdF_3 nanoplates. The crystal structure of GdF_3 nanoplates matches the orthorhombic phase (JCPDS# 49-1804). Peak broadening analysis reveals that (101), (301), and (002) reflections are sharper than other reflections, indicating that nanoplates are growing along the [101] direction and are confined by the (020) plane. This is consistent with the synthesis results conducted with a small addition of $^{90}YCl_3$ (Figure 1a–d), indicating that the same processes to yield specific morphologies are applicable in the isotopically labeled nanocrystals.

The growth mechanism with YCl_3 precursors is also investigated by taking the aliquots during the reaction at 320 °C without addition of $^{90}YCl_3$ and analyzing with TEM and PXRD. Figure 6a–f represents TEM images of nanocrystals synthesized using YCl_3 as precursors taken at 10 min intervals. After 10 min at 320 °C, nearly monodisperse spherical nanocrystals are observed. The PXRD data show that the crystal structure at this stage is orthorhombic YF_3 (Figure 7a). Continued growth at 320 °C results in shape transformation, as indicated in TEM images, from spheres to rhombic plates, rectangular plates, or wires. PXRD pattern indicates that the crystal structures are all still orthorhombic YF_3 (Figure 7b). As the reaction proceeds, the fraction of nanoplates or nanowires decreases relative to the amount of bypramidal-shaped nanocrystals, as observed in Figure 6d–f. After 60 min, only bipyramidal-shaped nanocrystals are observed. The XRD pattern

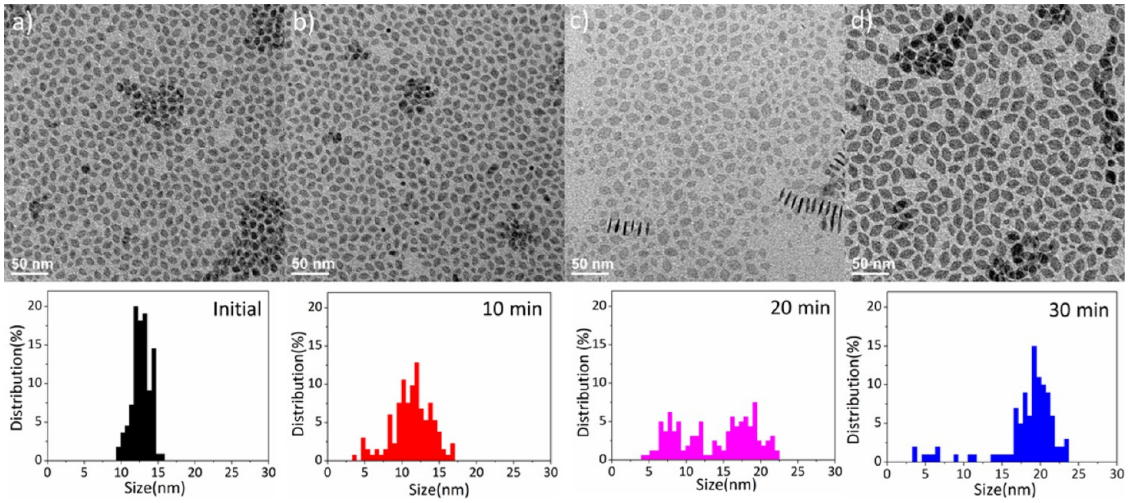

Figure 5. TEM images and tip-to-tip size distribution histograms of (a) purified ellipsoidal GdF_3 nanoplates used for the aging experiment and (b−d) after additional aging at 320 °C for 10, 20, and 30 min in the absence of Gd precursors.

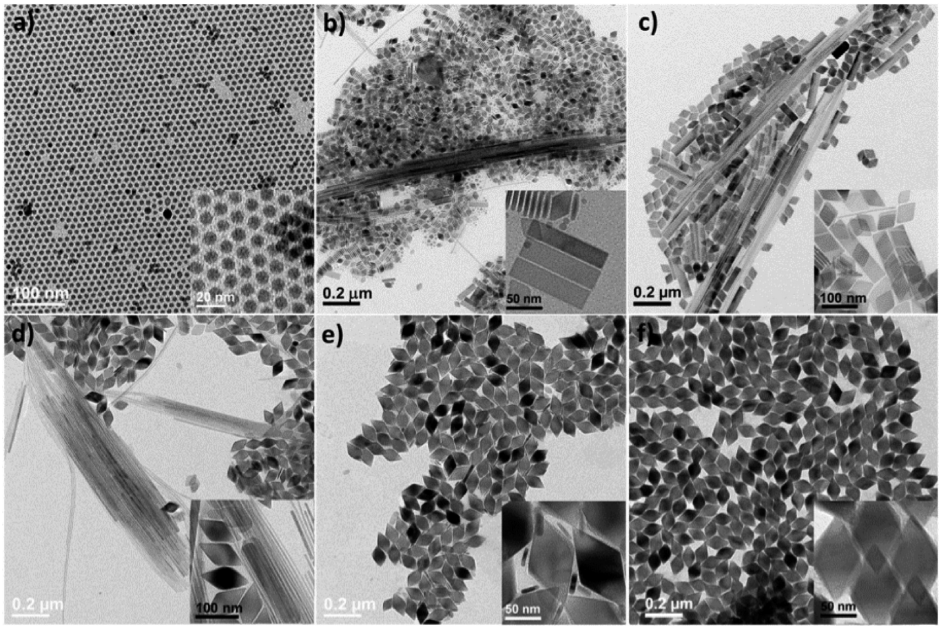

Figure 6. Size and morphology evolution during the reaction of YCl_3 and LiF. TEM images at (a) 10 min, (b) 20 min, (c) 30 min, (d) 40 min, (e) 50 min, and (f) 60 min reaction times at 320 °C.

indicates that the bipramidal-shaped nanocrystals are purely tetragonal $LiYF_4$ structures (Figure 7c). This trend also correlates the shape control of yttrium-based nanocrystals attained in the reaction process with radioisotope labeling, as displayed in Figure 1e−h. The morphology of the nanocrystals is also tuned by changing the ratios of LiF to YCl_3 under the same reaction conditions. Figure 8 shows TEM images after the reaction of YCl_3 and LiF at 320 °C for 20 min with different LiF to YCl_3 molar ratios. Rhombic nanoplates are formed preferentially at higher LiF to YCl_3 ratios, and the relative population of nanowires or elongated nanoplates increases as the LiF to YCl_3 ratio decreases.

Surface Modification of Radiolabeled GdF_3:^{90}Y/Y Nanocrystals by Ligand Exchange. As synthesized, radiolabeled nanocrystals are only soluble in nonpolar solvents such as hexane, toluene, and chloroform due to the long alkyl chain ligands on the surface. For biological compatibility, water-soluble ^{90}Y-doped nanocrystals are prepared *via* a two-step ligand exchange process using tetrafluoroborate anions (BF_4^-) as an intermediate ligand and water-soluble polymers as the final stabilizer.[40,61] Nitrosonium tetrafluoroborate ($NOBF_4$) is used to prepare BF_4^--capped GdF_3:^{90}Y/Y nanocrystals. Nitrosonium cations are known as strong oxidants and vigorously react with the nanocrystal surface, stripping the original oleate ligands from the nanocrystal surface. Figure 9 displays Fourier transform infrared (FT-IR) spectra before and after ligand exchanges with $NOBF_4$. The complete removal of C−H stretching vibrations at 2800−3000 cm^{-1} and an appearance of the

BF_4^- vibrational peak at 1085 cm^{-1} are observed after $NOBF_4$ treatment, indicating that BF_4^- ligands exchange the original oleic acid surfactants. We observed no loss of radioactivity from sample preparations following exposure to the highly chemically reactive environment of the $NOBF_4$ treatment, suggesting that ^{90}Y is strongly bound in the nanocrystal. Water-soluble polymers, polyethylenimine (PEI) and poly(acrylic acid) (PAA), are used for the secondary ligand exchange. After polymeric ligand treatments, the C−H vibrations around 2925 cm^{-1}, COO^- vibration around 1560 cm^{-1} (PAA ligands), and N−H vibrations around 3345 and 1630 cm^{-1} (PEI ligands) are observed due to the exchange from BF_4^- to polymeric ligands (Figure 9). Secondary ligand exchange with acidic and basic polymers did not result in loss of radioactivity, again suggesting chemically stable ^{90}Y-doping within the nanocrystal host.

Cellular Interaction of Radiolabeled Nanocrystals with Live Cells *in Vitro*. Radioisotopic labeling of nanoprobes allows quantitative tracing of these agents and enables the study of cellular interactions with high sensitivity. To demonstrate that our radiolabeled nanocrystals have potential to be utilized as an imaging agent to investigate the transport and localization of nanomaterials in biological system, we examine charge-dependent cellular binding of ^{90}Y-doped anisotropic GdF_3:^{90}Y/Y nanoplates, surface modified with differentially charged polymeric ligands (PEI and PAA). The size and size distribution of ligand-exchanged nanoplates is determined by dynamic light scattering (DLS) measurements. Although DLS defines the size of materials based on the assumption that the object has spherical morphology, DLS measurements provide a good indication of relative size and the size dispersion of anisotropic nanocrystals.[62] DLS data show that PEI- and PAA-modified GdF_3:^{90}Y/Y nanoplates used for *in vitro* studies are 32.4 and 33.9 nm in size, respectively, forming a stable dispersion in aqueous media without aggregation (Figure 10a). ζ-Potential measurements of PEI- and PAA-modified nanocrystals show positive and negative net charge in deionized water solution, respectively, due to the cationic ammonium and anionic carboxylate groups on the polymeric

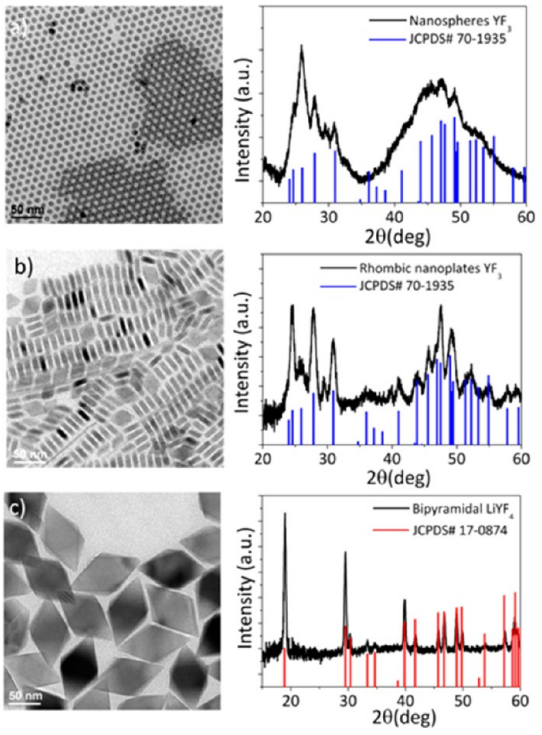

Figure 7. Representative TEM images and PXRD patterns of (a) spherical YF_3, (b) rhombic YF_3 nanoplates, and (c) bipyramidal $LiYF_4$.

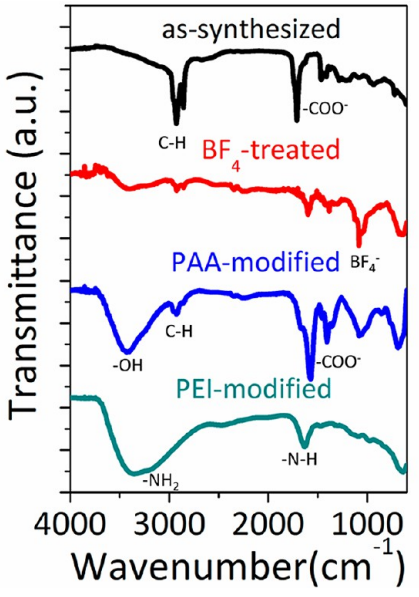

Figure 9. FT-IR spectra of GdF_3 nanoplates before and after ligand exchange with BF_4^-, PAA, and PEI.

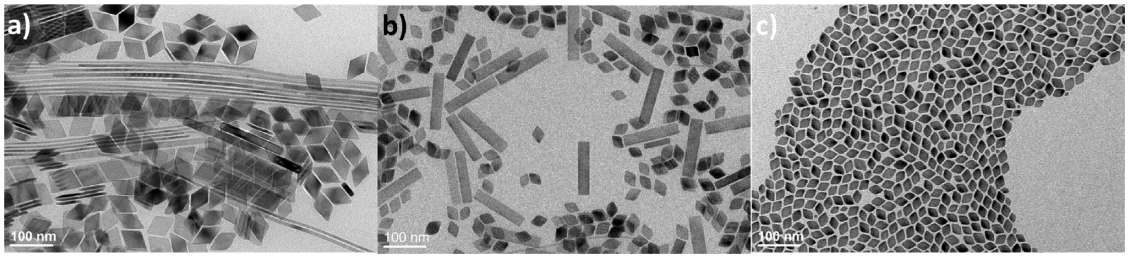

Figure 8. TEM images after the reaction of YCl_3 and LiF at 320 °C for 30 min under different molar ratios of LiF/YCl_3 ratio, (a) 9:1, (b) 12:1, and (c) 18:1.

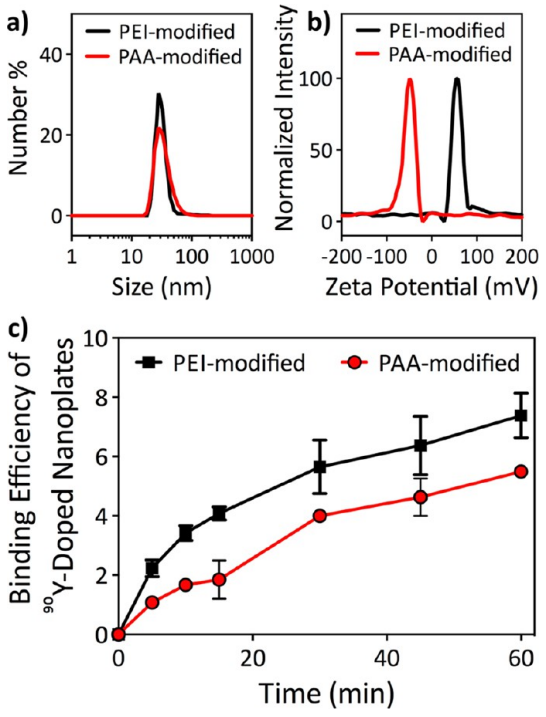

Figure 10. (a) DLS and (b) ζ-potential measurements of PEI- and PAA-modified ^{90}Y-doped GdF_3 nanoplates. (c) *In vitro* tracing of time-dependent binding of GdF_3:^{90}Y/Y nanoplates to HUVEC cells, with each time point run in quadruplicate. Black squares and red circles indicate binding efficiency of PEI- and PAA-modified GdF_3 nanoplates, respectively.

ligands (Figure 10b). To assess the interaction of the differentially charged nanoplates with biological membranes, a confluent monolayer of human umbilical vein endothelial cells (HUVECs) is used to model the systemic vasculature. ^{90}Y-doped GdF_3 nanoplates are formulated in serum-containing medium, and nanocrystal binding to cells is measured over time by γ counting. Unbound nanocrystals are removed by washing, and cell-bound radioactivity is normalized to the total radioactivity added (binding efficiency), as shown in Figure 9c. The amount of nanocrystal bound to cells is higher with positively charged PEI-modified nanocrystals than negatively charged PAA-coated ones. This result is likely due to the electrostatic attraction of positively charged PEI-modified particles to the negatively charged cell membrane, which is consistent with previously reported results.[52,63] In addition, the cellular binding and internalization of negatively charged particles on our cell model (HUVECs) may be inhibited by serum opsonization,[64] which might influence the particle−cellular interactions in serum-containing medium.

Imaging Cerenkov Optical Radioluminescense Emitted from GdF_3:^{90}Y/Y Nanoplates. We investigated the potential of GdF_3:^{90}Y/Y nanocrystals as optical imaging agents. The charged particle emitted from a radionuclide induces local polarization along its path, resulting in optical emission from near-ultraviolet to visible and near-infrared, known as Cerenkov radiation.[65] A variety of

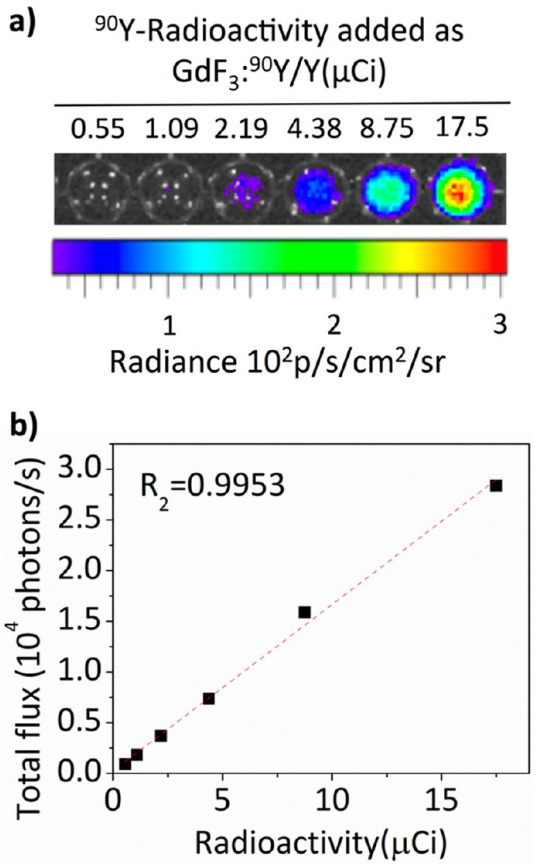

Figure 11. (a) Optical images of aqueous suspensions of GdF_3:^{90}Y/Y nanoplates with varying amounts of radioactivity per well (0.55 to 17.5 μCi). (b) Dose-dependent quantification of radioluminescence of GdF_3:^{90}Y/Y nanoplates dispersed in water.

radionuclides, including β^+, β^-, and γ emitters, have been demonstrated as *in vivo* real-time optical imaging agents.[30] Even though the amount of light emitted from the radionuclides is lower than that of bioluminescence and fluorescence, lack of excitation reduces autofluororescence from background fluorophores, resulting in significant increase in signal to background ratios.[66] Aqueous dilutions of ^{90}Y-doped nanocrystals with radioactivity ranging from 0.55 to 17.5 μCi per well are placed in a black-walled 96-well plate, and ^{90}Y radioluminescence was investigated using an IVIS Lumina II optical imaging system. Y-doped GdF_3 plates emit Cerenkov radiation from β decays. Figure 11 depicts the linear relationship between total radiance and radioactivity. This relationship suggests that our ^{90}Y-doped nanocrystals are applicable for quantitative optical imaging studies, as reported for other radiolabeled nanocrystal probes, such as ^{198}Au-doped Au nanocages.[22]

MRI Performance of GdF_3:^{90}Y/Y Nanoplates. Although nuclear and optical imaging techniques provide high sensitivity and means for quantification, these methods suffer from poor *in vivo* resolution. Magnetic resonance imaging (MRI) provides anatomical and

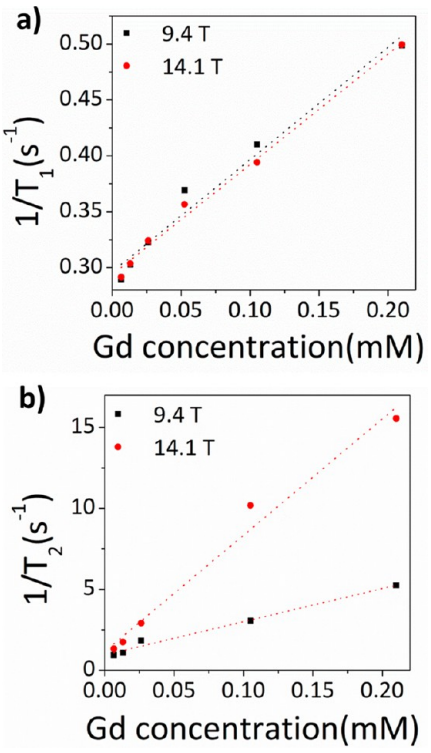

Figure 12. MR relaxivity measurements of PEI-modified ^{90}Y-doped GdF_3 nanoplates. (a) Longitudinal (r_1 = 0.99 mM^{-1} s^{-1} at 9.4 T and 1.0 mM^{-1} s^{-1} at 14.1 T) and (b) transverse relaxivity (r_2 = 20.3 mM^{-1} s^{-1} at 9.4 T and 71.8 mM^{-1} s^{-1} at 14.1 T) curves of PEI-modified GdF_3:^{90}Y/Y nanoplates.

functional information with high resolution of probe distribution.[11] This complementary imaging technique could be co-registered with nuclear and optical images to provide more reliable and comprehensive information on biological systems, albeit with lower sensitivity than nuclear and optical techniques. The synthesis of nanocrystals with the paramagnetic lanthanide elements such as Gd,[35,67] Eu,[68] and Dy[69,70] allows these lanthanide-based materials to be applicable for MRI contrast agents. MR relaxivity measurements of PEI-coated GdF_3:^{90}Y/Y nanoplates were performed using 9.4 and 14.1 T magnets. Ionic relaxivity plots of PEI-capped nanoplates are shown in Figure 12. The calculated longitudinal relaxivities (r_1) are 0.99 mM^{-1} s^{-1} at 9.4 T and 1.0 mM^{-1} s^{-1} at 14.1 T. The transverse relaxivities (r_2) are 20.3 mM^{-1} s^{-1} at 9.4 T and 71.8 mM^{-1} s^{-1} at 14.1 T. Calculated r_2/r_1 ratios are enhanced from 20.5 to 71.8 with an increase of field strength. For the next generation of MRI, higher magnetic fields (>7 T) are desirable to achieve improved signal-to-noise ratio, resulting in enhancement of spatial resolution, shortened scan times, and reduced concentrations of contrast dose.[69,71] High r_2 relaxivity and an enhanced r_2/r_1 ratio in increasing field strength make GdF_3 nanoplates promising T_2 contrast agents for high-field MRI, currently utilized for preclinical and biomedical research.

CONCLUSION

In summary, we demonstrate the size- and shape-controlled synthesis of ^{90}Y-doped rare earth fluoride nanocrystals. We observed that the shape of GdF_3:^{90}Y/Y nanoplates changes from ellipsoidal nanoplates to faceted rhombic shape during the reaction. When yttrium precursors are used, changes of shape and composition are observed. The morphology of nanocrystals evolves from YF_3:^{90}Y nanowires to $LiYF_4$:^{90}Y bipyramidal when enough energy is supplied during the longer reaction time. ^{90}Y-labeled nanocrystals show excellent radiolabel stability toward surface modification with different types of ligands. This provides the potential to further modify the surface with targeting or therapeutic moieties for biomedical imaging research. In addition, ^{90}Y-labeled GdF_3 nanoplates show radioluminescence attributed to Cerenkov radiation, which provides optical imaging capability. When combined with a paramagnetic gadolinium host, this nanocrystal can also be potentially utilized as an MRI contrast agent. Taken together, shape-controlled ^{90}Y-labeled nanocrystals are a promising platform for multimodal imaging applications.

METHODS

Materials. All chemicals are used as purchased without any further purification. Gadolinium chloride hexahydrate (99.999%), yttrium chloride hexahydrate (99.99%), lithium fluoride (99.99%), oleic acid (technical grade, 90%), and 1-octadecene (technical grade, 90%) are purchased from Sigma-Aldrich. $^{90}YCl_3$ solution (0.05 M HCl, ~500 Ci/mg) is purchased from PerkinElmer.

Synthesis of ^{90}Y/Y-Doped Rare Earth Fluoride Nanocrystals. ^{90}Y/Y-doped nanoplates (GdF_3:^{90}Y/Y, YF_3:^{90}Y/Y, $LiYF_4$:^{90}Y) are synthesized according to the procedure previously reported with slight modification.[57] Briefly, LiF (7.7 mmol) and $GdCl_3$ (0.7 mmol) or LiF (6.1 mmol) and YCl_3 (0.66 mmol) are added to a 125 mL three-neck flask containing an oleic acid and 1-octadecene mixture (50/50 vol %, 20 mL for $GdCl_3$ and 10 mL for YCl_3). This solution is degassed at 125 °C for 1 h. Then, a solution of $^{90}YCl_3$ (1−4 mCi, 22−89 nmol ^{90}Y in 0.05 M HCl) mixed with YCl_3 (0.2625 μL, 1.4 μmol in 0.05 M HCl) is added into the reaction mixture and degassed for an extra 30 min. Next, the solution is heated to 290−320 °C under an Ar environment at a rate of 10 °C/min and maintained at this temperature for 20 min to 1 h. Purification is conducted by precipitating nanocrystals in excess ethanol and centrifugation at 4000 rpm for 2 min. ^{90}Y-doped nanocrystals are redissolved in hexane. Residual lithium fluoride, which is insoluble in nonpolar solvents, is removed by centrifugation at 3000 rpm for 2 min. Radiochemical purity is assessed *via* digital autoradiography (FLA-7000, GE) of silica (SiO_2) TLC plates run in a water/methanol mixture (50/50 vol % with 5% ethylenediamine tetraacetic acid). Radiolabeled nanocrystals remain at the origin, while unbound ^{90}Y travels to the solvent front.

Preparation of Water-Soluble GdF_3:^{90}Y/Y Nanoplates. Water-soluble GdF_3:^{90}Y/Y nanoplates are prepared through a two-step sequential ligand exchange process using BF_4^- as an intermediate ligand. First, ligand exchange with $NOBF_4$ is performed, as described previously.[40,61] The resulting nanocrystals are

redissolved in dimethylformamide (DMF). Secondary ligand exchange is conducted with PEI, PVP, and PAA as water-soluble ligands. Two milliliters of nanocrystal solution in DMF is slowly added to 2 mL of polymer solution over 5 min and stirred for 30 min. Polymer concentrations are 0.3 mg/mL PEI in dimethyl sulfoxide, 0.3 mg/mL PAA in DMF, and 0.25 mg/mL PVP in DMF. Purification is conducted by adding nonsolvent in the nanocrystal solution, specifically toluene for PEI, acetonitrile and toluene mixture (9:1) for PAA, and hexanes for PVP, to induce flocculation. The particles are collected by centrifugation at 3000 rpm for 1 min. Nonsolvent is added until the solution becomes slightly opaque. Too much addition of nonsolvent results in the precipitation of polymers and is difficult to remove from the pure particles. Diluted HCl solution for PEI-capped and diluted NaOH for PAA-capped nanocrystals is added into the nanocrystal solution to increase colloidal stability. Confirmation of radiolabel stability is performed as described above.

Characterization. TEM images and electron diffraction patterns are recorded using a JEM-1400 microscope equipped with a SC1000 ORIUS CCD camera operating at 120 kV. HRTEM images are taken using a JEOL 2100 microscope operating at 200 kV. Scanning electron microscopy and energy-dispersive X-ray spectroscopy spectra are collected on a JEOL 7500F HRSEM equipped with an Oxford X-stream EDS detector. Dynamic light scattering is performed on a Zetasizer NanoS (Malvern). The ζ-potential data are collected on a Beckman Coulter Delsa Nano-C system. ^{90}Y radioluminescence is investigated using an IVIS Lumina II optical imaging system. Aqueous dilutions of PAA-modified GdF_3:^{90}Y/Y nanocrystals with radioactivity ranging from 0.55 to 17.5 μCi are placed in a black-walled 96-well plate and used for optical imaging. MR measurements are conducted by the method previously reported.[40,72,73]

Cellular Binding. Cellular binding assesments of GdF_3:^{90}Y/Y nanoplates are performed with PEI- or PAA-coated nanoplates prepared in assay buffer (cell media with 10% FBS diluted 1:1 with PBS). HUVEC cells are grown to confluence in a 1% gelatin-coated 96-well plate. Triplicate samples of ^{90}Y-doped nanoplates are incubated with cells at 37 °C for up to 1 h. Cells are washed three times with 3% BSA/PBS, and the radioactivity bound to cells is determined by a γ counter (Wizard^2 2470, PerkinElmer) in an open window using a standard for calibration.

Conflict of Interest: The authors declare no competing financial interest.

Acknowledgment. Primary support for the radiolabeled synthesis surface modification, X-ray analysis, microscopic analysis, and MR relaxivity measurements was provided by the National Science Foundation through the University of Pennsylvania's Nano/Bio Interface Center Grant No. DMR08-32802. The non-radioactive nanocrystal chemistry was developed with the support of Office of Naval Research Multidisciplinary University Research Initiative, under Award No. ONR-N00014-10-1-0942. A.M.C. and J.M. were supported by the National Center for Research Resources and the National Center for Advancing Translational Sciences, National Institutes of Health, through Grant KL2TR000139. J.F. was supported by the Daniel Sullivan Research Fund. C.B.M. is grateful for the support of the Richard Perry University Professorship.

Supporting Information Available: The Supporting Information is available free of charge on the ACS Publications website at DOI: 10.1021/acsnano.5b03355.

Additional radioTLC results (PDF)

REFERENCES AND NOTES

1. Nel, A. E.; Mädler, L.; Velegol, D.; Xia, T.; Hoek, E. M. V.; Somasundaran, P.; Klaessig, F.; Castranova, V.; Thompson, M. Understanding Biophysicochemical Interactions at the Nano-Bio Interface. *Nat. Mater.* **2009**, *8*, 543–557.
2. Chithrani, B. D.; Chan, W. C. W. Elucidating the Mechanism of Cellular Uptake and Removal of Protein-Coated Gold Nanoparticles of Different Sizes and Shapes. *Nano Lett.* **2007**, *7*, 1542–1550.
3. Verma, A.; Uzun, O.; Hu, Y.; Hu, Y.; Han, H.-S.; Watson, N.; Chen, S.; Irvine, D. J.; Stellacci, F. Surface-Structure-Regulated Cell-Membrane Penetration by Monolayer-Protected Nanoparticles. *Nat. Mater.* **2008**, *7*, 588–595.
4. Yoon, T.-J.; Lee, H.; Shao, H.; Weisslede, R. Highly Magnetic Core-Shell Nanoparticles with a Unique Magnetization Mechanism. *Angew. Chem., Int. Ed.* **2011**, *50*, 4663–4666.
5. Gambhir, S. S. Molecular Imaging of Cancer with Positron Emission Tomography. *Nat. Rev. Cancer* **2002**, *2*, 683–693.
6. Gao, X.; Cui, Y.; Levenson, R. M.; Chung, L. W. K.; Nie, S. *In vivo* Cancer Targeting and Imaging with Semiconductor Quantum Dots. *Nat. Biotechnol.* **2004**, *22*, 969–976.
7. Weissleder, R.; Pittet, M. J. Imaging in the Era of Molecular Oncology. *Nature* **2008**, *452*, 580–589.
8. Liu, Y.; Welch, M. J. Nanoparticles Labeled with Positron Emitting Nuclides: Advantages, Methods, and Applications. *Bioconjugate Chem.* **2012**, *23*, 671–682.
9. Cho, E. C.; Glaus, C.; Chen, J.; Welch, M. J.; Xia, Y. Inorganic Nanoparticle-Based Contrast Agents for Molecular Imaging. *Trends Mol. Med.* **2010**, *16*, 561–573.
10. Kim, J.; Piao, Y.; Hyeon, T. Multifunctional Nanostructured Materials for Multimodal Imaging, and Simultaneous Imaging and Therapy. *Chem. Soc. Rev.* **2009**, *38*, 372–390.
11. Louie, A. Multimodality Imaging Probes: Design and Challenges. *Chem. Rev.* **2010**, *110*, 3146–3195.
12. Burda, C.; Chen, X.; Narayanan, R.; El-Sayed, M. A. Chemistry and Properties of Nanocrystals of Different Shapes. *Chem. Rev.* **2005**, *105*, 1025–1102.
13. Huh, Y.-M.; Jun, Y.-w.; Song, H.-T.; Kim, S.; Choi, J.-s.; Lee, J.-H.; Yoon, S.; Kim, K.-S.; Shin, J.-S.; Suh, J.-S.; et al. *In Vivo* Magnetic Resonance Detection of Cancer by Using Multifunctional Magnetic Nanocrystals. *J. Am. Chem. Soc.* **2005**, *127*, 12387–12391.
14. Michalet, X.; Pinaud, F. F.; Bentolila, L. A.; Tsay, J. M.; Doose, S.; Li, J. J.; Sundaresan, G.; Wu, A. M.; Gambhir, S. S.; Weiss, S. Quantum Dots for Live Cells, *in Vivo* Imaging, and Diagnostics. *Science* **2005**, *307*, 538–544.
15. Mai, H.-X.; Zhang, Y.-W.; Si, R.; Yan, Z.-G.; Sun, L.-d.; You, L.-P.; Yan, C.-H. High-Quality Sodium Rare-Earth Fluoride Nanocrystals: Controlled Synthesis and Optical Properties. *J. Am. Chem. Soc.* **2006**, *128*, 6426–6436.
16. Wong, R. M.; Gilbert, D. A.; Liu, K.; Louie, A. Y. Rapid Size-Controlled Synthesis of Dextran-Coated, ^{64}Cu-Doped Iron Oxide Nanoparticles. *ACS Nano* **2012**, *6*, 3461–3467.
17. Sun, X.; Huang, X.; Guo, J.; Zhu, W.; Ding, Y.; Niu, G.; Wang, A.; Kiesewetter, D. O.; Wang, Z. L.; Sun, S.; et al. Self-Illuminating ^{64}Cu-Doped CdSe/ZnS Nanocrystals for *in Vivo* Tumor Imaging. *J. Am. Chem. Soc.* **2014**, *136*, 1706–1709.
18. Freund, B.; Tromsdorf, U. I.; Bruns, O. T.; Heine, M.; Giemsa, A.; Bartelt, A.; Salmen, S. C.; Raabe, N.; Heeren, J.; Ittrich, H.; et al. A Simple and Widely Applicable Method to ^{59}Fe-Radiolabel Monodisperse Superparamagnetic Iron Oxide Nanoparticles for *in Vivo* Quantification Studies. *ACS Nano* **2012**, *6*, 7318–7325.
19. Marmorato, P.; Simonelli, F.; Abbas, K.; Kozempel, J.; Holzwarth, U.; Franchini, F.; Ponti, J.; Gibson, N.; Rossi, F. ^{56}Co-Labelled Radioactive Fe_3O_4 Nanoparticles for *in Vitro* Uptake Studies on Balb/3T3 and Caco-2 Cell Lines. *J. Nanopart. Res.* **2011**, *13*, 6707–6717.
20. Yang, Y.; Sun, Y.; Cao, T.; Peng, J.; Liu, Y.; Wu, Y.; Feng, W.; Zhang, Y.; Li, F. Hydrothermal Synthesis of $NaLuF_4$:^{153}Sm, Yb,Tm Nanoparticles and Their Application in Dual-Modality Upconversion Luminescence and SPECT Bioimaging. *Biomaterials* **2013**, *34*, 774–783.
21. Sun, Y.; Zhu, X.; Peng, J.; Li, F. Core−Shell Lanthanide Upconversion Nanophosphors as Four-Modal Probes for Tumor Angiogenesis Imaging. *ACS Nano* **2013**, *7*, 11290–11300.
22. Wang, Y.; Liu, Y.; Luehmann, H.; Xia, X.; Wan, D.; Cutler, C.; Xia, Y. Radioluminescent Gold Nanocages with Controlled Radioactivity for Real-Time *in Vivo* Imaging. *Nano Lett.* **2013**, *13*, 581–585.

23. Shao, X.; Agarwal, A.; Rajian, J. R.; Kotov, N. A.; Wang, X. Synthesis and Bioevaluation of ^{125}I-Labeled Gold Nanorod. *Nanotechnology* **2011**, *22*, 135102.
24. Sun, Y.; Yu, M.; Liang, S.; Zhang, Y.; Li, C.; Mou, T.; Yang, W.; Zhang, X.; Li, B.; Huang, C.; et al. Fluorine-18 Labeled Rare-Earth Nanoparticles for Positron Emission Tomography (PET) Imaging of Sentinel Lymph Node. *Biomaterials* **2011**, *32*, 2999–3007.
25. Liu, Q.; Sun, Y.; Li, C.; Zhou, J.; Li, C.; Yang, T.; Zhang, X.; Yi, T.; Wu, D.; Li, F. 18F-Labeled Magnetic-Upconversion Nanophosphors via Rare-Earth Cation-Assisted Ligand Assembly. *ACS Nano* **2011**, *5*, 3146–3157.
26. Cremonesi, M.; Ferrari, M.; Paganelli, G.; Rossi, A.; Chinol, M.; Bartolomei, M.; Prisco, G.; Tosi, G. Radiation Protection in Radionuclide Therapies with ^{90}Y-Conjugates: Risks and Safety. *Eur. J. Nucl. Med. Mol. Imaging* **2006**, *33*, 1321–1327.
27. Giammarile, F.; Bodei, L.; Chiesa, C.; Flux, G.; Forrer, F.; Kraeber-Bodere, F.; Brans, B.; Lambert, B.; Konijnenberg, M.; Borson-Chazot, F.; et al. EANM Procedure Guideline for the Treatment of Liver Cancer and Liver Metastases with Intra-Arterial Radioactive Compounds. *Eur. J. Nucl. Med. Mol. Imaging* **2011**, *38*, 1393–1406.
28. Lhommel, R.; van Elmbt, L.; Goffette, P.; Van den Eynde, M.; Jamar, F.; Pauwels, S.; Walrand, S. Feasibility of ^{90}Y TOF PET-Based Dosimetry in Liver Metastasis Therapy Using SIR-Spheres. *Eur. J. Nucl. Med. Mol. Imaging* **2010**, *37*, 1654–62.
29. Elschot, M.; Vermolen, B. J.; Lam, M. G.; de Keizer, B.; van den Bosch, M. A.; de Jong, H. W. Quantitative Comparison of PET and Bremsstrahlung SPECT for Imaging the *in Vivo* Yttrium-90 Microsphere Distribution After Liver Radioembolization. *PLoS One* **2013**, *8*, e55742.
30. Liu, H.; Ren, G.; Miao, Z.; Zhang, X.; Tang, X.; Han, P.; Gambhir, S. S.; Cheng, Z. Molecular Optical Imaging with Radioactive Probes. *PLoS One* **2010**, *5*, e9470.
31. Nyk, M.; Kumar, R.; Ohulchanskyy, T. Y.; Bergey, E. J.; Prasad, P. N. High Contrast *in Vitro* and *in Vivo* Photoluminescence Bioimaging Using Near Infrared to Near Infrared Up-Conversion in Tm^{3+} and Yb^{3+} Doped Fluoride Nanophosphors. *Nano Lett.* **2008**, *8*, 3834–3838.
32. Park, Y. I.; Lee, K. T.; Suh, Y. D.; Hyeon, T. Upconverting Nanoparticles: a Versatile Platform for Wide-Field Two-Photon Microscopy and Multi-Modal *In Vivo* Imaging. *Chem. Soc. Rev.* **2015**, *44*, 1302–1317.
33. Chen, G.; Qiu, H.; Prasad, P. N.; Chen, X. Upconversion Nanoparticles: Design, Nanochemistry, and Applications in Theranostics. *Chem. Rev.* **2014**, *114*, 5161–5214.
34. Carpenter, C. M.; Sun, C.; Pratx, G.; Liu, H.; Cheng, Z.; Xing, L. Radioluminescent Nanophosphors Enable Multiplexed Small-Animal Imaging. *Opt. Express* **2012**, *20*, 11598–11604.
35. Johnson, N. J. J.; Oakden, W.; Stanisz, G. J.; Prosser, R. S.; van Veggel, F. C. J. M. Size-Tunable, Ultrasmall $NaGdF_4$ Nanoparticles: Insights into Their T_1 MRI Contrast Enhancement. *Chem. Mater.* **2011**, *23*, 3714–3722.
36. Yuan, D.; Tan, M. C.; Riman, R. E.; Chow, G. M. Comprehensive Study on the Size Effects of the Optical Properties of $NaYF_4$:Yb,Er Nanocrystals. *J. Phys. Chem. C* **2013**, *117*, 13297–13304.
37. Shan, J.; Uddi, M.; Wei, R.; Yao, N.; Ju, Y. The Hidden Effects of Particle Shape and Criteria for Evaluating the Upconversion Luminescence of the Lanthanide Doped Nanophosphors. *J. Phys. Chem. C* **2010**, *114*, 2452–2461.
38. Wang, F.; Liu, X. Upconversion Multicolor Fine-Tuning: Visible to Near-Infrared Emission from Lanthanide-Doped $NaYF_4$ Nanoparticles. *J. Am. Chem. Soc.* **2008**, *130*, 5642–5643.
39. Ye, X.; Collins, J. E.; Kang, Y.; Chen, J.; Chen, D. T. N.; Yodh, A. G.; Murray, C. B. Morphologically Controlled Synthesis of Colloidal Upconversion Nanophosphors and Their Shape-Directed Self-Assembly. *Proc. Natl. Acad. Sci. U. S. A.* **2010**, *107*, 22430–22435.
40. Paik, T.; Gordon, T. R.; Prantner, A. M.; Yun, H.; Murray, C. B. Designing Tripodal and Triangular Gadolinium Oxide Nanoplates and Self-Assembled Nanofibrils as Potential Multimodal Bioimaging Probes. *ACS Nano* **2013**, *7*, 2850–2859.
41. Zhang, Q.; Yan, B. Hydrothermal Synthesis and Characterization of $LiREF_4$ (RE = Y, Tb-Lu) Nanocrystals and Their Core-Shell Nanostructures. *Inorg. Chem.* **2010**, *49*, 6834–6839.
42. Si, R.; Zhang, Y.-W.; You, L.-P.; Yan, C.-H. Rare-Earth Oxide Nanopolyhedra, Nanoplates, and Nanodisks. *Angew. Chem., Int. Ed.* **2005**, *44*, 3256–3260.
43. Wang, F.; Han, Y.; Lim, C. S.; Lu, Y.; Wang, J.; Xu, J.; Chen, H.; Zhang, C.; Hong, M.; Liu, X. Simultaneous Phase and Size Control of Upconversion Nanocrystals Through Lanthanide Doping. *Nature* **2010**, *463*, 1061–1065.
44. Wang, F.; Liu, X. Recent Advances in the Chemistry of Lanthanide-Doped Upconversion Nanocrystals. *Chem. Soc. Rev.* **2009**, *38*, 976–989.
45. Jiang, W.; Kim, B. Y. S.; Rutka, J. T.; Chan, W. C. W. Nanoparticle-Mediated Cellular Response Is Size-Dependent. *Nat. Nanotechnol.* **2008**, *3*, 145–150.
46. Adriani, G.; de Tullio, M. D.; Ferrari, M.; Hussain, F.; Pascazio, G.; Liu, X.; Decuzzi, P. The Preferential Targeting of the Diseased Microvasculature by Disk-like Particles. *Biomaterials* **2012**, *33*, 5504–5513.
47. Black, K. C. L.; Wang, Y.; Luehmann, H. P.; Cai, X.; Xing, W.; Pang, B.; Zhao, Y.; Cutler, C. S.; Wang, L. V.; Liu, Y.; et al. Radioactive ^{198}Au-Doped Nanostructures with Different Shapes for *In Vivo* Analyses of Their Biodistribution, Tumor Uptake, and Intratumoral Distribution. *ACS Nano* **2014**, *8*, 4385–4394.
48. Dasgupta, S.; Auth, T.; Gompper, G. Shape and Orientation Matter for the Cellular Uptake of Nonspherical Particles. *Nano Lett.* **2014**, *14*, 687–693.
49. Albanese, A.; Tang, P. S.; Chan, W. C. W. The Effect of Nanoparticle Size, Shape, and Surface Chemistry on Biological Systems. *Annu. Rev. Biomed. Eng.* **2012**, *14*, 1.
50. Derfus, A. M.; Chan, W. C. W.; Bhatia, S. N. Probing the Cytotoxicity of Semiconductor Quantum Dots. *Nano Lett.* **2004**, *4*, 11.
51. Nel, A.; Xia, T.; Mädler, L.; Li, N. Toxic Potential of Materials at the Nanolevel. *Science* **2006**, *311*, 622–627.
52. Alkilany, A. M.; Nagaria, P. K.; Hexel, C. R.; Shaw, T. J.; Murphy, C. J.; Wyatt, M. D. Cellular Uptake and Cytotoxicity of Gold Nanorods: Molecular Origin of Cytotoxicity and Surface Effects. *Small* **2009**, *5*, 701–708.
53. Colvin, V. L. The Potential Environmental Impact of Engineered Nanomaterials. *Nat. Biotechnol.* **2003**, *21*, 1166–1170.
54. Ye, X.; Chen, J.; Engel, M.; Millan, J. A.; Li, W.; Qi, L.; Xing, G.; Collins, J. E.; Kagan, C. R.; Li, J.; et al. Competition of Shape and Interaction Patchiness for Self-Assembling Nanoplates. *Nat. Chem.* **2013**, *5*, 466–473.
55. Sun, X.; Zhang, Y.-W.; Du, Y.-P.; Yan, Z.-G.; Si, R.; You, L.-P.; Yan, C.-H. From Trifluoroacetate Complex Precursors to Monodisperse Rare-Earth Fluoride and Oxyfluoride Nanocrystals with Diverse Shapes through Controlled Fluorination in Solution Phase. *Chem.—Eur. J.* **2007**, *13*, 2320–2332.
56. Boyer, J.-C.; Cuccia, L. A.; Capobianco, J. A. Synthesis of Colloidal Upconverting NaYF4:Er^{3+}/Yb^{3+} and Tm^{3+}/Yb^{3+} Monodisperse Nanocrystals. *Nano Lett.* **2007**, *7*, 847–852.
57. Paik, T.; Ko, D.-K.; Gordon, T. R.; Doan-Nguyen, V.; Murray, C. B. Studies of Liquid Crystalline Self-Assembly of GdF_3 Nanoplates by In-Plane, Out-of-Plane SAXS. *ACS Nano* **2011**, *5*, 8322–8330.
58. Johnson, N. J. J.; Korinek, A.; Dong, C.; van Veggel, F. C. J. M. Self-Focusing by Ostwald Ripening: A Strategy for Layer-by-Layer Epitaxial Growth on Upconverting Nanocrystals. *J. Am. Chem. Soc.* **2012**, *134*, 11068–11071.
59. Rinkel, T.; Nordmann, J.; Raj, A. N.; Haase, M. Ostwald-Ripening and Particle Size Focussing of Sub-10 nm $NaYF_4$ Upconversion Nanocrystals. *Nanoscale* **2014**, *6*, 14523–14530.
60. Jia, G.; Sitt, A.; Hitin, G. B.; Hadar, I.; Bekenstein, Y.; Amit, Y.; Popov, I.; Banin, U. Couples of Colloidal Semiconductor Nanorods Formed by Self-Limited Assembly. *Nat. Mater.* **2014**, *13*, 301–307.

61. Dong, A.; Ye, X.; Chen, J.; Kang, Y.; Gordon, T.; Kikkawa, J. M.; Murray, C. B. A Generalized Ligand-Exchange Strategy Enabling Sequential Surface Functionalization of Colloidal Nanocrystals. *J. Am. Chem. Soc.* **2011**, *133*, 998–1006.
62. Ji, Z.; Wang, X.; Zhang, H.; Lin, S.; Meng, H.; Sun, B.; George, S.; Xia, T.; Nel, A. E.; Zink, J. I. Designed Synthesis of CeO_2 Nanorods and Nanowires for Studying Toxicological Effects of High Aspect Ratio Nanomaterials. *ACS Nano* **2012**, *6*, 5366–5380.
63. Verma, A.; Stellacci, F. Effect of Surface Properties on Nanoparticle−Cell Interactions. *Small* **2010**, *6*, 12–21.
64. Serda, R. E.; Gu, J.; Bhavane, R. C.; Liu, X.; Chiappini, C.; Decuzzi, P.; Ferrari, M. The Association of Silicon Microparticles with Endothelial Cells in Drug Delivery to the Vasculature. *Biomaterials* **2009**, *30*, 2440–2448.
65. Robertson, R.; Germanos, M. S.; Li, C.; Mitchell, G. S.; Cherry, S. R.; Silva, M. D. Optical Imaging of Cerenkov Light Generation from Positron-Emitting Radiotracers. *Phys. Med. Biol.* **2009**, *54*, N355–N365.
66. Thorek, D. L.; Robertson, R.; Bacchus, W. A.; Hahn, J.; Rothberg, J.; Beattie, B. J.; Grimm, J. Cerenkov Imaging - a New Modality for Molecular Imaging. *Am. J. Nucl. Med. Mol. Imaging* **2012**, *2*, 163–173.
67. Park, Y. I.; Kim, J. H.; Lee, K. T.; Jeon, K.-S.; Na, H. B.; Yu, J. H.; Kim, H. M.; Lee, N.; Choi, S. H.; Baik, S.-I.; et al. Nonblinking and Nonbleaching Upconverting Nanoparticles as an Optical Imaging Nanoprobe and T_1 Magnetic Resonance Imaging Contrast Agent. *Adv. Mater.* **2009**, *21*, 4467–4471.
68. Kattel, K.; Park, J. Y.; Xu, W.; Kim, H. G.; Lee, E. J.; Bony, B. A.; Heo, W. C.; Lee, J. J.; Jin, S.; Baeck, J. S.; et al. A Facile Synthesis, *In Vitro* and *In Vivo* MR Studies of d-Glucuronic Acid-Coated Ultrasmall Ln_2O_3 (Ln = Eu, Gd, Dy, Ho, and Er) Nanoparticles as a New Potential MRI Contrast Agent. *ACS Appl. Mater. Interfaces* **2011**, *3*, 3325–3334.
69. Das, G. K.; Johnson, N. J. J.; Cramen, J.; Blasiak, B.; Latta, P.; Tomanek, B.; van Veggel, F. C. J. M. $NaDyF_4$ Nanoparticles as T_2 Contrast Agents for Ultrahigh Field Magnetic Resonance Imaging. *J. Phys. Chem. Lett.* **2012**, *3*, 524–529.
70. Das, G. K.; Zhang, Y.; D'Silva, L.; Padmanabhan, P.; Heng, B. C.; Loo, J. S. C.; Selvan, S. T.; Bhakoo, K. K.; Tan, T. T. Y. Single-Phase Dy_2O_3:Tb^{3+} Nanocrystals as Dual-Modal Contrast Agent for High Field Magnetic Resonance and Optical Imaging. *Chem. Mater.* **2011**, *23*, 2439–2446.
71. Bottrill, M.; Kwok, L.; Long, N. J. Lanthanides in Magnetic Resonance Imaging. *Chem. Soc. Rev.* **2006**, *35*, 557–571.
72. Lauffer, R. B. Paramagnetic Metal Complexes as Water Proton Relaxation Agents for NMR Imaging: Theory and Design. *Chem. Rev.* **1987**, *87*, 901–927.
73. Eykyn, T. R.; Payne, G. S.; Leach, M. O. Inversion Recovery Measurements in the Presence of Radiation Damping and Implications for Evaluating Contrast Agents in Magnetic Resonance. *Phys. Med. Biol.* **2005**, *50*, N371–N376.